Available online at www.sciencedirect.com
ScienceDirect
Trans. Nonferrous Met. Soc. China 33(2023) 3067−3082
Transactions of Nonferrous Metals Society of China
www.tnmsc.cn

Effect of square wave potential polarity and amplitude on property of trivalent chromium conversion coating applied on Zn−Al hot-dip coating

Jie PAN*, Yang CHENG*, Ya-jing DING, Rui-cheng ZHAO, Tao JIANG, Zhen-liang FENG, Yan LI

School of Materials Science and Engineering, China University of Petroleum (East China), Qingdao 266580, China

Received 12 March 2022; accepted 1 September 2022

Abstract: The formation of Cr(III) chemical conversion coating (TCC) on Zn−Al hot-dip coating was unraveled and cathode or anode square wave potential (φ_p) was applied during the TCC construction progress in terms of comparatively investigating the effectiveness of φ_p. Corrosion resistance of TCC in chloride-containing solution was obtained by EIS and polarization curve measurements, combined with the discussion of macro/micro-morphology using 3D microscope and chemical composition distribution analysis using XPS, AES, FTIR and Raman spectra. The results showed that the cathode φ_p enhanced the corrosion resistance and reduced the content of Cr(VI) on the surface of freshly-prepared TCC better than anode φ_p. Besides, the hydrophobicity of TCC and adhesion to epoxy primer were also improved due to the reconstruction of the micro−nano structure.

Key words: hot-dip coating; Cr(III) conversion coating; wave potential; surface roughness

1 Introduction

As one of the main protective alloy coatings on steel sheets, galvanized coating plays an important role in the sustainable development of automobile manufacturing industry, agriculture and ocean engineering. With the higher pursuit of corrosion resistance, the multiple-phase hot-dip Zn−Al alloy coating with 55 wt.% Al addition has been one of the best choices for protecting carbon steel substrate with unique appearance since the 1960s [1,2]. Galvanized coating can provide good cathode protection for steel substrate which has a lightweight design in terms of energy conservation, emission reduction and cost saving [3]. The researchers have studied the corrosion behavior and mechanism of Zn−Al alloy coating [4,5] and Zn−Al−Mg alloy coating [6,7] in chlorine/sulfur containing corrosive media or atmospheric environment [8], including cross section [9,10] and different corrosion periods [11]. It has been proven that hot-dip Zn−Al coating was very sensitive to pitting in severe corrosive environment such as high chlorine or alternating wet−dry thin liquid film coverage [12,13]. Therefore, it is an efficient way to pre-treat the surface before developing more tolerant coating system and chemical conversion coating is one of the most crucial methods to improve the temporary corrosion resistance and adhesion to primers.

Although the traditional hexavalent chromium Cr(VI) conversion coating (CCC) has excellent corrosion resistance, Cr(VI) as a harmful carcinogen is explicitly prohibited by many environmental regulations, i.e., RoHS [14,15]. Therefore, trivalent chromium Cr(III) chemical conversion coating (TCC) and chromium free chemical conversion coating become the future oriented pretreatment process. At present, TCC has been proven to be the best choice to replace CCC and has been successfully applied on the surface

* These authors contributed equally to this work

Corresponding author: Yan LI, Tel: +86-13615321199, E-mail: yanlee@upc.edu.cn

DOI: 10.1016/S1003-6326(23)66318-6

of Zn alloy [16], Al alloy [17,18], Zn−Al−Mg coating [6] and galvanized coating [19,20]. Due to the condition that fresh formed TCC would appear in some Cr(VI) compounds, further limiting the trace Cr(VI) in TCC has arisen the attention in this research field. At present, relevant works have reported the various new conversion coating techniques including organosilane modified method [21], silsesquioxane-modified graphene oxide-incorporated method [22], rare earth [23] or lanthanide element oxygen-containing anion based bath [24] in order to replace CCC. But application of TCC is still plunging into the depth of people.

Differently from Al or Zn alloys, previous results [5] indicated a selectivity activity of the zinc rich interdendritic region (IDR) in acid environments compared to the aluminum rich dendritic region (DR), and this is then proven and discussed detailedly by ZHANG et al [4]. Therefore, this kind of non-uniform dissolution could also reasonably complicate the performance of Zn55Al during the process of chemical conversion, which may lead to the integrity and uniformity of TCC ensured by appropriate regulation methods.

Previously, we selected Zn−55%Al−1.6%Si (hereinafter referred to as Zn55Al) and carried out a systematically physicochemical and electrochemical research on the construction and performance of TCC [20]. In this work, based on the 3D surface morphology, surface and in depth distribution of chemical composition, the feasibility of external electro field regulation on TCC was discussed. The effect of anode square-wave potential φ_p is further explored in addition to the cathode φ_p by changing the polarity and amplitude in terms of corrosion resistance and Cr(VI) content on fresh formed TCC. Through the analysis of surface roughness, the relationship among the contact angle value, primer adhesion strength and the calculated surface energy was established.

2 Experimental

2.1 Materials and construction of conversion coating

Commercial passivator Alodine 5928 (Henkel, Germany), which contains 1−10 wt.% trivalent chromium salt and 0.1−1 wt.% fluorozirconate compounds, was diluted with deionized (DI) water to prepare 50 vol.% solution at pH 2.7. After being degreased with ultrasonic cleaning in acetone and rinsing with DI water, the TCCs were constructed by immersing 50 mm × 50 mm Zn55Al panels in the Cr(III) chemical conversion process (TCP) bath at 40 °C for 180 s which is regarded as the optimal treating time [20], followed by a final DI water rinse in a glass beaker.

The polarity and amplitude of anode or cathode square-wave potential φ_p were set to be ±0.05, ±0.10 and ±0.20 V (vs Ag/AgCl during the TCP process). Accordingly, the measured average current densities when applying cathode φ_p were -1.60×10^{-3}, -3.50×10^{-3}, and -8.00×10^{-3} A/cm^2, and the current densities applying anodic φ_p were 2.80×10^{-3}, 5.30×10^{-3} and 1.10×10^{-2} A/cm^2, respectively. The frequency of the applied φ_p was 5 Hz, and the duty ratio was 0.2 s:0.2 s. When the deposition began, the open circuit potential dropped rapidly and gradually stabilized at −0.92 V vs Ag/AgCl at ~20 s, then the pulse potential was applied to the sheets, and the total deposition time was 180 s.

The oxidation−reduction potential (ORP) parameters and pH value of TCP bath were determined by Quanta (HACH, USA) portable water quality analyzer using standard platinum electrode and Ag/AgCl reference electrode. The monitoring distance of the chemical conversion solution parameter detection probe was always kept at ~2 cm away from the sample under a solution stirring with 100 r/min.

2.2 Chemical and micro-morphological characterization

The morphology of the coating was examined by field-emission high-resolution scanning electron microscopy (JSM−7200F, Japan) with energy-dispersive X-ray (EDS) spectroscopy at 15 keV. X-ray photoelectron spectra were recorded using an ESCALAB 250Xi spectrometer (ThermoFisher USA) with an Al K_α X-ray source. The micro focus monochromator was operated at a spot size of ~400 μm, including DR and IDR on TCC. In order to mitigate the influence of air pollutants and excess carbon on the test results, the Ar^+ ion sputtering depth was 5 nm and all data were corrected by C 1s binding energy at 284.8 eV.

AES measurements were performed on PHI 710 scanning auger nanoprobe (ULVAC−PHI, Japan) with a tungsten filament electron emission

source. A cylindrical mirror analyzer (CMA) was adopted and the test beam energy used for stimulating specimen signals and SEM imaging was 10 kV, and the current was 10 nA. All the Auger electron spectra were acquired with an energy analyzer resolution of <0.5%. The surface was sputtered using a 2.0 keV Ar^+ ion beam over an area of 2.0 mm × 2.0 mm and the emission current was 3.0 mA/cm^2. The recorded spectra were analyzed with Multipak V9.0 software and the characteristic peak of element C (275.0 eV) was used for the calibration. The instrument used for Raman spectroscopy is a Horiba lab−RAM HR Evolution (HORIBA France) instrument. Argon ion laser was used as the laser (λ=514.5 nm, and the output laser power was 1.0 MW). LWD50× was used as the objective lens, and the acquisition time was 30 s, which had been accumulated three times.

2.3 Surface roughness and contact angle measurement

The Zeta−20A 3D profiler instrument (Zeta Instruments, USA) was used to observe the 3D morphology and to compare the surface roughness of TCC with different immersion time. The field of view was 1164 μm × 873 μm. Surface profiles were obtained, repeatedly scanning a line extending from the untreated regions over the TCP-treated regions using a 10× objective lens with a scanning distance of 150 μm. The roughness R_a was calculated by Zeta3D software (version 1.7.5), which is the arithmetic mean of the absolute ordinate values $Z(x)$ ($R_a = 1/l \int_0^l |Z(x)| \mathrm{d}x$) within the sampling length according to the ISO 12085. The contact angles of 4 μL pure water drops were measured by a contact angle goniometer (XG−CAMC, China) at room temperature to investigate the surface hydrophilicity. Samples were carefully air-cleaned to avoid surface contamination.

A pull-off adhesion tester (PosiTest AT−A, USA) was used following a direct pull-off standardized procedure according to ASTM D4541 to study the effects of surface roughness and texture on the adhesion of the epoxy zinc yellow primer to Zn55Al. The dolly size was ~20 mm and the pull rate was controlled at a speed of 0.2 MPa/s. All specimens were kept at ambient temperature for at least 24 h in laboratory air to ensure that the glue fully cured before the test.

2.4 Corrosion and electrochemical measurements

All electrochemical measurements were conducted using an Autolab PGSTAT302F potentiostat (Metrohm AG, Switzerland). The measurements were made in air-saturated 0.5 mol/L NaCl solution at room temperature. The counter electrode was a pure Pt electrode with 2 cm^2 working area, and the reference was an Ag/AgCl electrode (saturated KCl). The potentiodynamic scans were recorded at 0.16 mV/s with a limit from −60 to 60 mV (vs φ_{ocp}). The polarization curves with low polarized domain were fitted by three parameters fitting method according to Butler−Volmer polarization curve equation. The EIS measurements were carried out in a frequency range of 10^{-2}−10^5 Hz, and the sinusoidal potential perturbation was 5 mV and Nova software (version 2.1.3) was used to fit the experimental data. EIS and Tafel polarization measurements were carried out once the monitored φ_{ocp} was steady after ~20 min. Scanning vibrating electrode technique (SVET) measurements were performed using an M370 scanning electrochemical workstation (Uniscan Instruments, UK), using 0.05 mol/L NaCl + 0.05 mol/L Na_2SO_4 corrosion solution. The purpose of adding Na_2SO_4 was to increase the conductivity of the electrolyte to enhance the sensitivity of detective probe. Half of the sample was immersed in the chemical conversion solution to prepare TCC with the assistance of φ_p regulation, while the other half was in the degreased state, and this created a natural dividing line as a result. The scan velocity was 10 μm/s, and the scanning probe was placed within 50 μm from the sample surface.

3 Results

3.1 Process and mechanism of TCC construction

The most intuitive feature at the beginning of TCC construction on Zn55Al is the mixed potential change of anode and cathode reaction that can be monitored by open circuit potential (OCP) in Fig. 1. Due to the coupling of two-phase on Zn55Al, a large number of cathode and anode micro reactions were formed. Figure 1 firstly showed a rapid and then a smooth downward trend with some turbulences. At the initial stage of TCP, a rapid decrease of φ_{ocp} from above −0.895 V to below −0.930 V vs Ag/AgCl was detected within 10 s. According to the previous mainstream research of

TCC on aluminum alloy, the change of φ_{ocp} during this period was attributed to the activation of fluoride on the substrate surface [25−28]. Then, the φ_{ocp} gradually decreased until the end of the TCP with continuous fluctuation of ~0.005 V, and finally the TCC with a stable state was constructed.

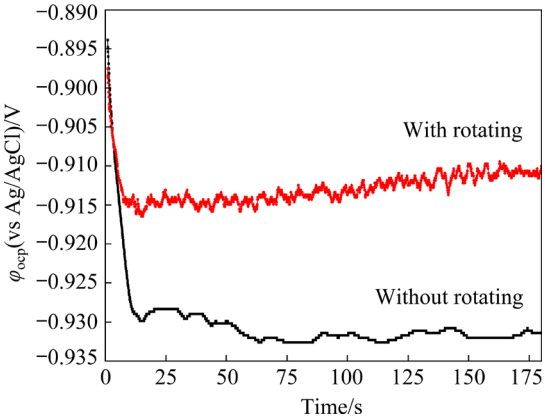

Fig. 1 Change of OCP as function of time in whole process of TCP with and without solution rotating

The following reactions were preferentially carried out at the same time in both the cathode and anode regions [29,30]:

Cathode reactions

$$2H^{+}+2e\rightarrow H_2 \quad (1)$$

$$O_2+2H_2O+4e\rightarrow 4OH^{-} \quad (2)$$

Anode reactions

$$M_{Zn,Al}\rightarrow M^{n+}_{Zn,Al}+ne \quad (3)$$

Since the beginning of TCP, the surface aluminum oxide film and aluminum matrix were continuously activated under the action of strong oxidation fluoride [31]. Due to the low bath pH, a lot of dissolved Zn^{2+} combined with the hydroxyl groups to form the alkaline hydroxide, which was firstly deposited at the initial TCC formation points on cathode regions [5,32]. However, the mass fraction of Al in Zn55Al coating is 55 wt.%, which means that Al-rich cathode region with lighter density occupies most of the surface. Preferential dissolution of Zn and precipitation of its hydroxide may block the cathode reactions somehow, but with the proceed of chemical conversion, new anode and cathode regions emerge constantly, which leads to the fluctuation of potential change.

When 200 r/min solution rotating was applied to the TCP, the φ_{ocp} tended to be stable near −0.910 V vs Ag/AgCl, which was slightly higher than that of the stationary solution. This meant that the construction of TCC was less stable and the surface was active during the whole TCP. And the measured dissolved oxygen (DO) content of the conversion bath under agitation was 22.19 mg/L, higher than 6.72 mg/L of the static bath, which may increase the risk of Cr(III) oxidation. Therefore, high flow rate of the TCP solution is not conducive to the construction of the TCC.

Lower bath pH is the key to surface activation and also the power source of TCP. The change of mean pH value and oxidation−reduction potential (ORP) of the TCP bath near the TCC formation surface is shown in Fig. 2. The concentration of OH^{-} ion in the TCP bath increased due to cathode Reactions (1)−(2), which was consistent with the increase of pH value. This allowed the precipitation of Zr(IV) and Cr(III) hydroxides with the hydrolysis of the soluble fluorometalate precursor species, leading to the formation of a hydrated metal oxide coating [33]:

$$M^{n+}_{Al,Zn,Cr}+nOH^{-}\rightarrow M_{Al,Zn,Cr}(OH)_n \quad (4)$$

$$ZrF_6^{2-}+4H_2O\rightarrow ZrO_2\cdot 2H_2O+6F^{-} \quad (5)$$

During 180 s TCP period, the increase of pH value is similar to that of the previous report [34], but ORP of the solution shows a significant contrary trend. ORP reflects the oxidizability of TCP bath. It can be seen that with the consumption of activated substances and the increase of pH value, the efficiency of TCC construction gradually decreases. To some extent, ORP value can be used as another index to evaluate the activity of the bath. Figure S1 in Supporting Information (SI) also shows the relationship between ORP and solution

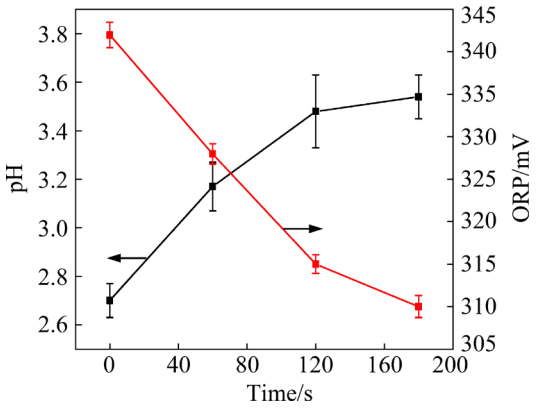

Fig. 2 Change of pH and ORP as function of time during whole process of TCP

temperature. From 34 to 37 ℃, the redox potential fluctuated sharply, which reflected the change in the ratios of oxide and reducing substance. It is necessary to avoid the unstable temperature range or to conduct chemical conversion reaction after the diluted solution is stable.

3.2 Surface morphology and element distribution of TCC

The SEM image and EDS mapping analysis of TCC surface under the optimal TCP parameters are shown in Fig. 3. The coarse micro-cracks distributing along the edge of DR could be observed. Interestingly, the elements related to the composition of TCC were more concentrated in these regions, which indicated that the transition region between DRs provided more film-forming active points. Many studies on the aluminum alloys also recorded larger thickness of conversion coatings on the dispersed intermetallic compounds (IMCs) and their edges [35−37]. The activation and dissolution of Zn or Al elements with different activity in acidic chemical conversion bath would produce a relatively strong local galvanic current, and this continuous power could be assumed stronger in the transition region [14].

In fact, at the initial stage of TCC construction, the micro-cracks were reflected on the edge of raised DR. EDS and SEM micro morphology analysis expressed this detailed in Fig. S2 in SI. Therefore, transition region between DR and IDR had the fastest film-forming speed and also very sensitive to micro-cracks. So, it is particularly critical to regulate the film-forming speed in order to avoid the possible decline of corrosion resistance caused by large amount of micro-cracks.

Figure 4 reveals the AES cross section distribution spectra acquired in DR. The signals of Al and Zn were stronger at the deeper ion sputtering depth, while the signal of O was stronger at the

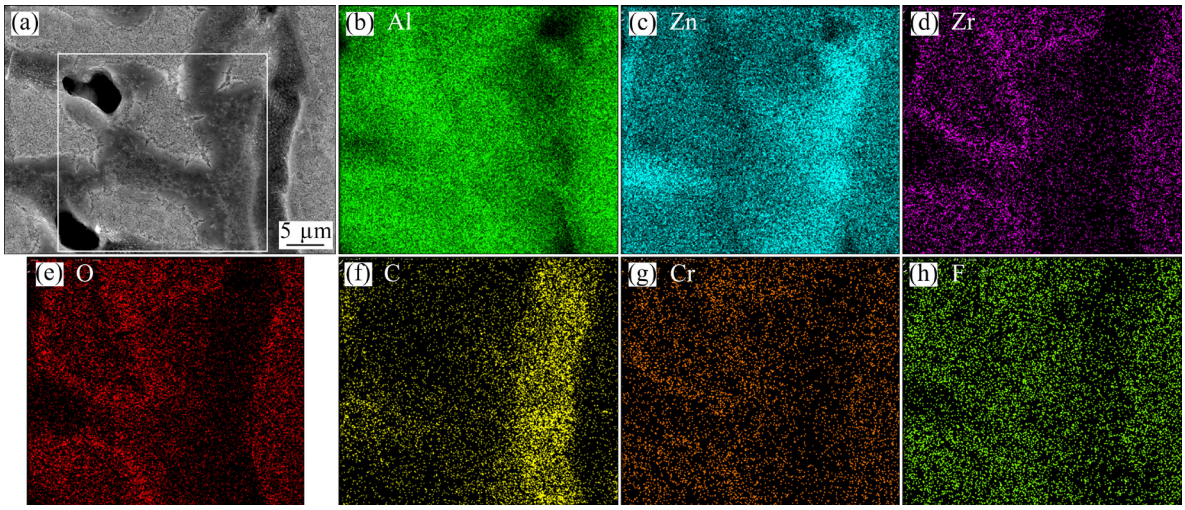

Fig. 3 SEM image (a) and EDS mappings (b−h) of main elements on TCC with TCP time of 180 s

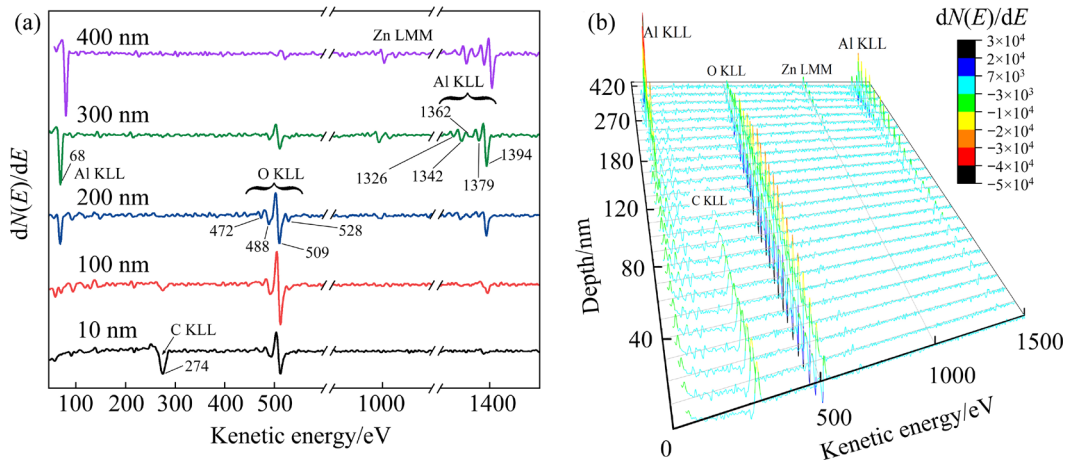

Fig. 4 AES survey spectra acquired at dendrite region: (a) Full spectrum; (b) Detailed distribution

middle level. This indicated that the middle layer (50−300 nm) without obvious stratification of TCC was probably mostly composed of oxides. Figure S3 in SI further confirmed this and showed that the TCC thickness of the raised Al-rich DR was smaller but denser than that of the IDR.

In Fig. 5(a), the unique micro−nano structure on the surface of TCC could be seen clearly. As previously analyzed, the surface of TCC was mostly composed of oxides with different film-forming elements. In IDR as shown in Fig. 5(b), there were micro-pores with different sizes of <100 nm, which may be caused by the preferential solution of zinc-rich particles in the acidic conversion bath. On DR as shown in Fig. 5(c), the size of micro-cracks was less than 1 μm. Based on the cross-sectional morphology in Fig. 5(e), the depth of the micro-crack was close to the thickness of the TCC. Dense distribution of micro cracks on the DR detected by AES in Fig. 5(f) greatly weakened the durability of the TCC in corrosive media containing Cl^-. According to previous studies, the formation of micro-cracks may be caused by the dehydration of the TCC and SEM observation in vacuum environment would undoubtedly aggravate it. However, the surface morphology of multiple cracks obviously restricted the performance of TCC. It is very important to optimize the surface integrity by using other composite additives or external field control.

3.3 Microstructure and composition of TCC regulated by φ_p

3.3.1 Surface microstructure with different φ_p

The detailed micro-morphology of TCC regulated by φ_p is shown in Fig. 6. It can be seen that, the transition region between the raised DR and the IDR presented a brighter view. During the TCP, the number and size of micro cracks on Zn55Al sample further decreased with the cathode φ_p compared with anode φ_p, especially when the amplitude was −0.1 V. At higher applied potential, more textured micro-bumps grew on the surface of TCC.

Figure 7 shows the 3D morphology and the roughness of TCC regulated with different φ_p. When φ_p=−0.20 V, the mean micro roughness R_a at DR increased by ~2.10 times, while the corresponding height difference R_z between DR and IDR decreased. Under the regulation of φ_p, the macro-roughness of TCC decreased while the local micro-roughness increased compared with the original topography of Zn55Al. The corresponding contact angle value with φ_p=−0.2 V increased to 112.30°, which provided the TCC with a hydrophobic behavior.

3.3.2 Surface composition with different φ_p

The distribution of main elements on the surface of the fresh TCC formed under different anode or cathode φ_p is shown in full XPS spectra in Fig. 8. Correspondingly, the molar fractions after

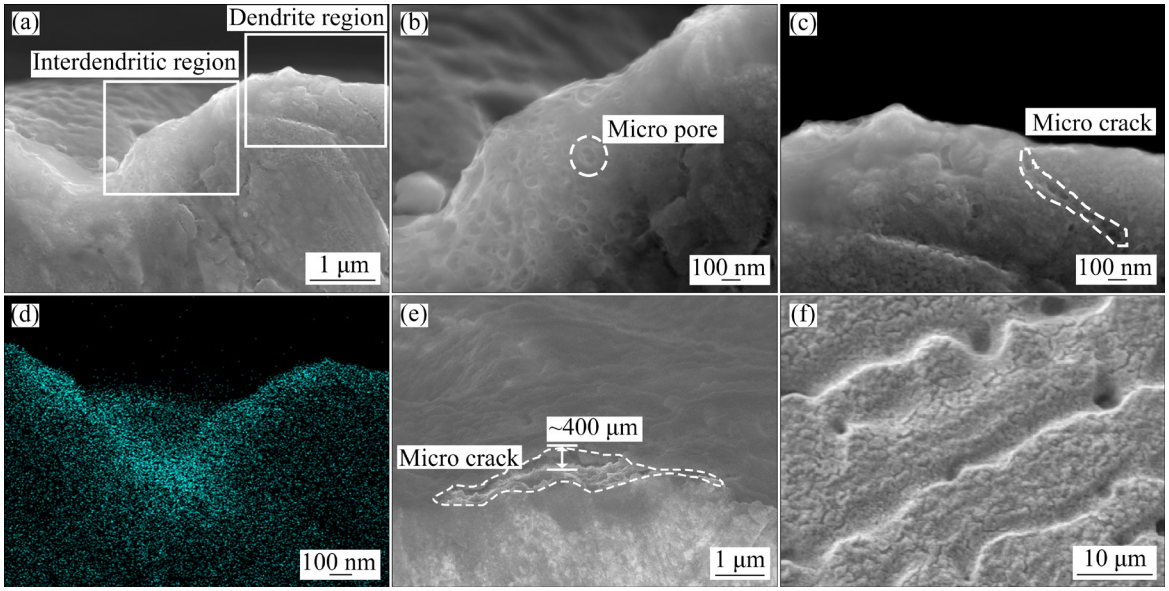

Fig. 5 Micro-morphology and EDS mapping analysis of DR and IDR on TCC with TCP time of 180 s: (a) Cross section containing both regions; (b) Micro pores on interdendritic region; (c) Micro cracks on dendritic region; (d) O element distribution; (e) Micro crack with ~400 μm in thickness; (f) Micrograph with Ar^+ ion sputtering for 30 min

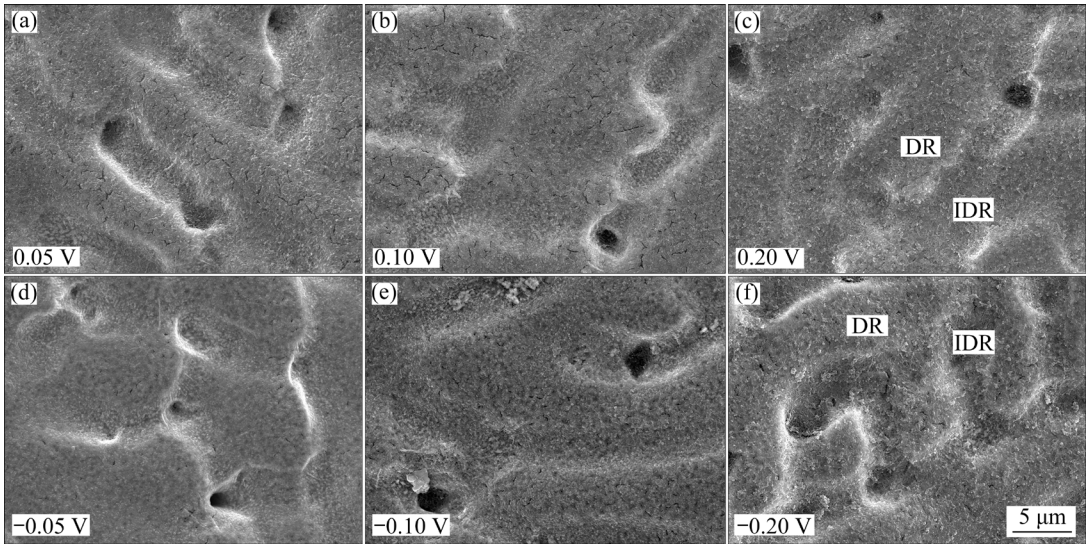

Fig. 6 Detailed surface micro-morphology of TCC-coated Zn55Al samples with effect of φ_p adopting positive potentials vs OCP (a−c) and negative potentials vs OCP (e−f) (Brighter region is the transition area between IDR and DR)

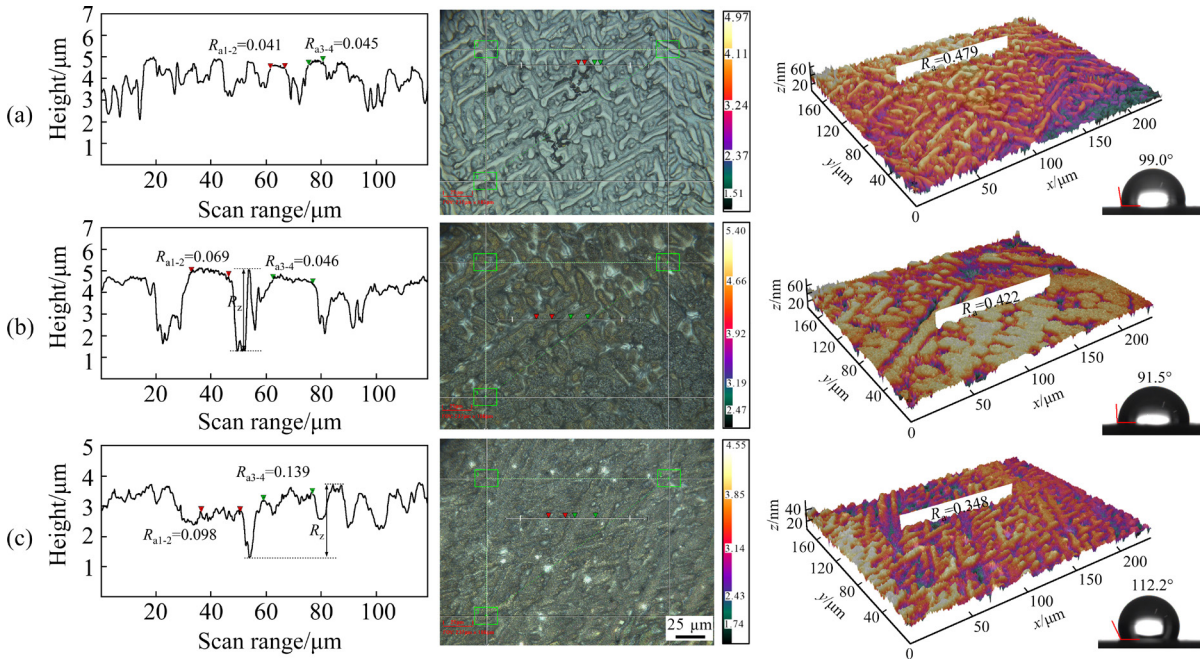

Fig. 7 Surface topography, corresponding roughness and contact angle measurement results of TCC-coated Zn55Al samples with regulation of different φ_p: (a) Degreased sample; (b) φ_p=0 V; (c) φ_p=−0.20 V

correction of C content are listed in Table 1. The XPS detection result included several DRs and IDRs, which was a reliable average mean value. The results showed that the signal of Cr, Zr, Al and F elements significantly increased by applying φ_p regulation during the TCP, especially when the cathode potential φ_p was applied.

For zirconium based TCC, one of the limiting factors and concerns is the valence of chromium in the newly constructed TCC. The XPS high-resolution spectra and fitting results of Cr $2p_{3/2}$ are shown in Fig. 9(a) and Table 2, respectively. Peaks were used to fit intensity in the region of 570.0−590.0 eV, including $Cr(OH)_3$ (577.2±0.2) eV, Cr_2O_3 (575.3±0.2) eV, Cr(VI) oxides (578.3±0.2) eV and CrF_3 (580.1±0.2) eV [38−40]. As the detection depth of XPS was ~5 nm, the results validated that the regulation of φ_p further reduced the trace content of Cr(VI) on the surface of TCC, especially when the cathode was applied. When φ_p=−0.20 V, the Cr(VI) component on newly constructed TCC was reduced by 30.20%, which was less effective

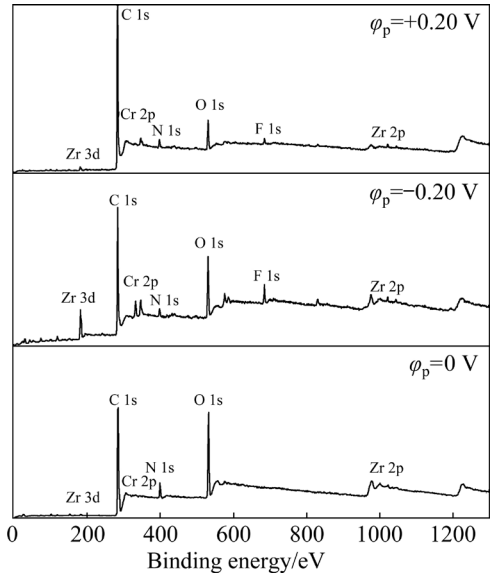

Fig. 8 XPS full spectra of TCC regulated by φ_p during TCP

Table 1 Main elements content on TCC surface regulated by different φ_p (at.%)

φ_p/V	O 1s	N 1s	Cr 2p	Zr 3d	Al 2p	Zn 2p	F 1s
0	76.50	17.19	1.46	0.31	2.71	0.65	1.17
−0.20	37.91	40.39	3.07	4.19	7.00	0.64	6.80
+0.20	33.89	57.80	1.29	0.76	2.24	0.84	3.18

compared to the decrease of 34.99% reported using −0.10 V previously [41]. With the increase of chromium content, the decrease of harmful Cr(VI) fully proved the effectiveness of φ_p regulation. Although anode potential also had some effect, it was not as obvious as cathode potential. This result provided a crucial new idea: it is feasible to control the construction process of TCC through external electric field in terms of environment-friendliness. However, the parameters of electric field need to be further adjusted and optimized.

The XPS high-resolution spectra of Zr $3d_{5/2}$ are shown in Fig. 9(b) and Table S1 in SI respectively. ZrO_2 (182.7±0.2) eV, $Zr(OH)_4$ (184.0±0.2) eV and ZrF_4 (185.3±0.2) eV for Zr $3d_{5/2}$ were used to fit the curve [20,38,42]. Also, the presence of Al_2O_3-I, Al_2O_3-II, $Al(OH)_3$ and AlF_3 was indicated by the Al $2p_{3/2}$ peaks at (73.0±0.2) eV, (74.7±0.2) eV, (73.9±0.2) eV and (76.3±0.2) eV, respectively, in Table S2 in SI and Fig. 9(c) [20,38]. The results revealed that the chemical forms of Zr and Al were mainly corresponding oxides, and φ_p regulation had unobvious effect on the proportion of Zr oxides and hydroxides. On the contrary, under the influence of external electric field, the hydroxide composition of Cr greatly increased, especially when cathode φ_p was applied. By analyzing the O 1s data in Fig. 9(d) and Table 3, it was proven that the general proportion of OH^- on the surface of TCC greatly increased by 52.46% after applying the cathode φ_p. As analyzed by SABABI et al [43] and FOCKAERT et al [44], the appearance of alkaline hydroxide on the surface of TCC could play an important role in regulating the surface free energy and improving the adhesion with subsequent epoxy primers.

3.4 Electrochemical properties of TCC regulated by φ_p

3.4.1 Polarization measurement under narrow polarized domain

According to the results of the previous section, the thickness of the TCC constructed on the surface of Zn55Al was not particularly thick (≤500 nm); considering the sensitivity of TCC to strong polarization, the method of polarization measurement under narrow polarized domain was preferred. Figure 10(a) shows the polarization curves of TCC regulated under different cathode φ_p during the TCP. Because there was no Tafel zone by nonlinear fitting in the range from −0.06 to 0.06 V vs Ag/AgCl, the most accurate fitting parameters could be obtained with electrochemical kinetic equation [45]:

$$J=J_{corr}\left[\exp\frac{2.303(\varphi-\varphi_{corr})}{b_a}\right]-\left[\exp\frac{-2.303(\varphi-\varphi_{corr})}{b_c}\right] \quad (6)$$

where φ_{corr} is the corrosion potential, J_{corr} is the corrosion current density, b_a and b_c are fitting coefficients.

According to the fitting results of dynamic parameters listed in Table 4, the corrosion resistance of TCC was improved by applying the cathode φ_p during the TCP, and the lowest corrosion current density J_{corr} was 4.68×10^{-8} A/cm^2 when the pulse potential φ_p=−0.10 V. Compared with the sample without φ_p, the corrosion current density of the TCC decreased by nearly an order of magnitude. The results showed that better corrosion resistance

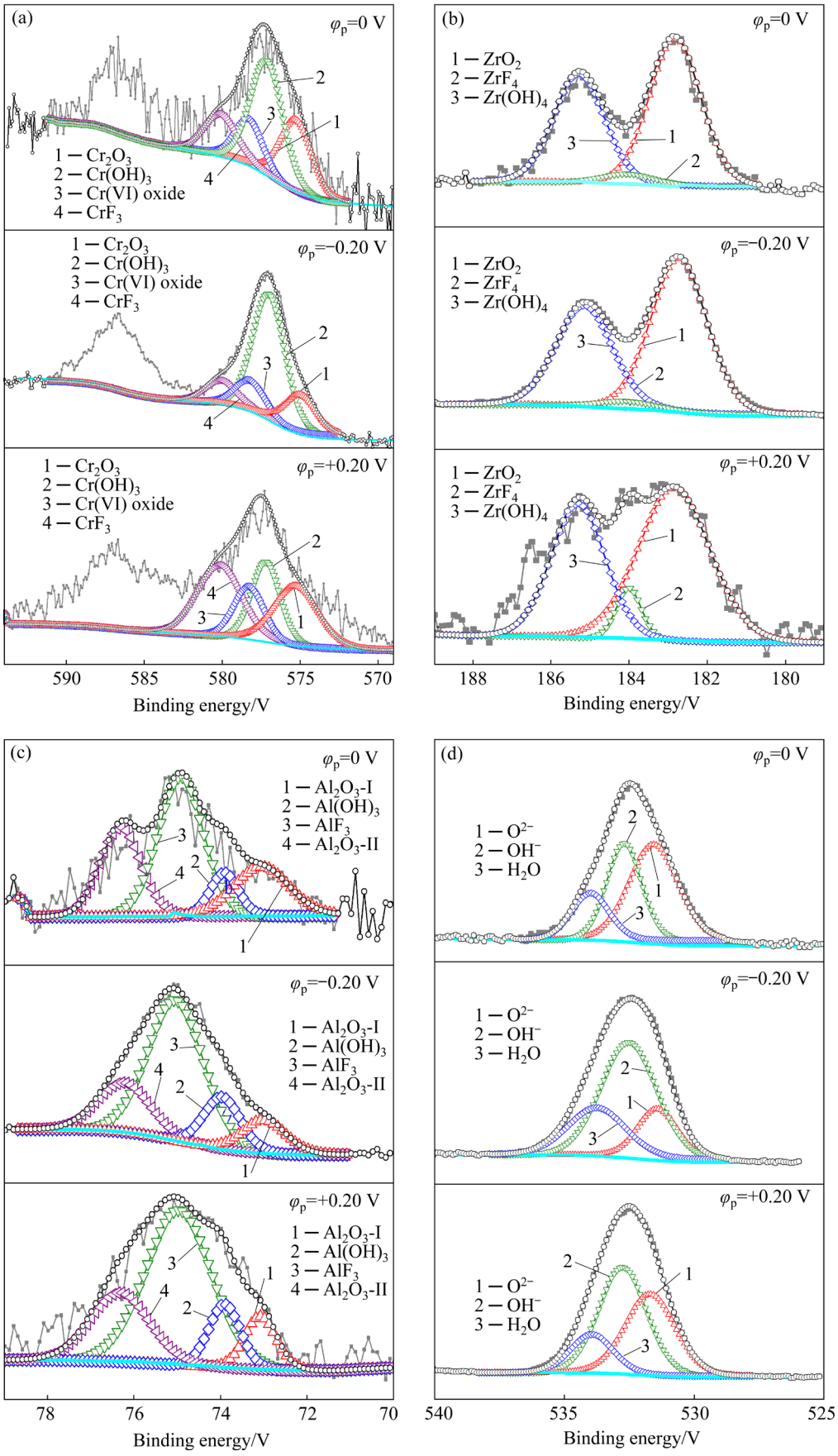

Fig. 9 Fitting results of Cr $2p_{3/2}$ (a), Zr $3d_{5/2}$ (b), Al $2p_{3/2}$ (c) and O 1s (d) on surface of TCCs regulated by different φ_p during TCP

Table 2 Proportion of different Cr $2p_{3/2}$ species on surface of TCCs with different φ_p (%)

φ_p/V	Cr_2O_3	$Cr(OH)_3$	Cr(VI) oxide	CrF_3
0	25.50	23.34	18.51	32.62
−0.20	17.60	58.84	12.92	10.65
+0.20	27.20	42.98	14.57	15.25

Table 3 Proportion of different O 1s species on surface of TCCs with different φ_p (%)

φ_p/V	O^{2-}	OH^-	H_2O
0	47.16	37.65	15.18
−0.20	17.18	57.40	24.82
+0.20	47.93	34.25	17.82

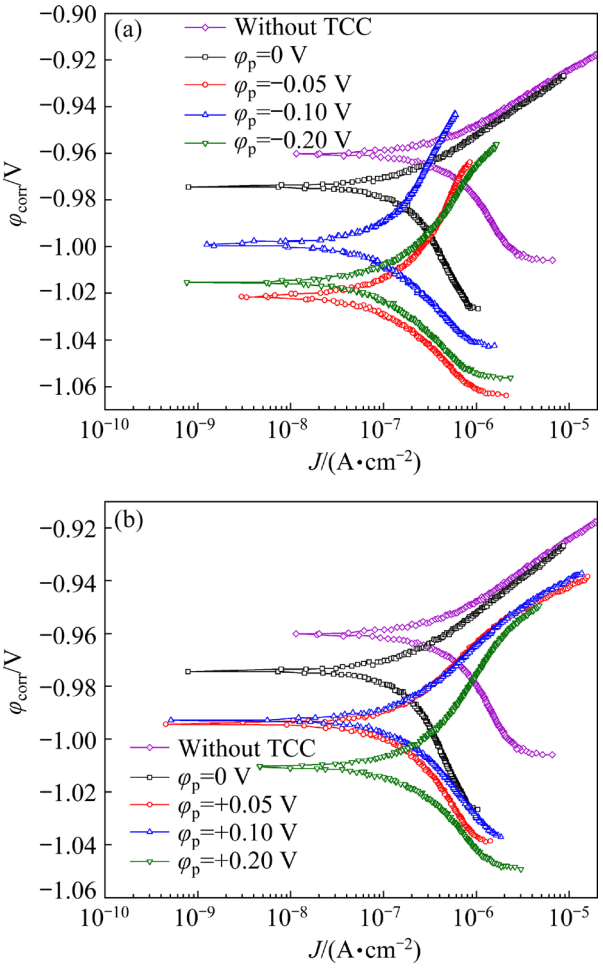

Fig. 10 Polarization curves of TCCs in 0.5 mol/L NaCl solution regulated by cathode φ_p (a) and anodic φ_p (b) during TCP

could be obtained by applying cathode φ_p. However, as shown in Fig. 10(b) and Table 4, the corrosion current density was 3.30×10^{-7} A/cm^2 when the positive φ_p of +0.05 V was adopted. It seems that anode φ_p could also appropriately reduce the J_{corr} value, but this may have great limitations. Anode φ_p accelerated the activation of Zn−Al surface during TCP, but it may indirectly reduce the density of TCC with the increase of thickness. Figure 6 comparatively showed that the application of φ_p of 0.1 V caused coarser micro cracks on the surface of TCC compared with −0.1 V. Of course, the detailed effect of other option of amplitude and polarity on improvement of corrosion resistance needs further investigation.

Table 4 Kinetic parameters for polarization curves of TCCs regulated by cathode φ_p

φ_p/V	φ_{corr}/V	J_{corr}/(A·cm^{-2})	b_a/(mV·dec^{-1})	$-b_c$/(mV·dec^{-1})
Without TCC	−0.96	2.11×10^{-6}	34.1	69.4
0	−0.97	6.59×10^{-7}	52.9	293.6
−0.05	−1.02	2.64×10^{-7}	99.3	91.3
−0.10	−1.01	4.68×10^{-8}	35.4	35.0
−0.20	−1.02	1.24×10^{-7}	65.6	67.9
+0.05	−0.99	3.30×10^{-7}	58.1	124.9
+0.10	−0.99	3.58×10^{-7}	58.0	108.1
+0.20	−1.01	3.98×10^{-7}	66.3	82.2

The values of Adj. R obtained in the non-linear fitting of weak polarization curves is over 0.990

3.4.2 EIS measurement

Figures 11(a, b) show the Nyquist and Bode diagrams of TCCs regulated with different cathode φ_p during the TCP. According to the characteristics of EIS, the equivalent circuit with two time constants was used to fit the electrochemical impedance test results [19,46]. R_s is the solution resistance; C_{dl} is the electric double layer capacitance; R_{ct} is the charge transfer resistance; $R_{pore,sol}$ and C_f are the reaction resistance and capacitance of the porous TCC, respectively. In addition, EIS data of TCC constructed under the regulation of anode φ_p is shown in Fig. S4 in SI. In the low-frequency domain of impedance, there was an obvious phenomenon of diffusion impedance, so the Warburg impedance W was added in the equivalent circuit for these samples. In fact, it can be seen from Fig. 5 that the TCC on the surface of Zn55Al conformed to the surface characteristics of porous electrode, and these macro pores could be

seen as semi-infinite diffusion physical model in the initial process of corrosion. The regulation of anode φ_p highlighted the diffusion phenomenon of TCC surface in corrosive electrolyte somehow.

Figure 11(a) showed that when the pulse square wave potential φ_p=−0.10 V, the values of the real part in Nyquist diagram and lg |Z| in Bode diagram were the largest, indicating that the corrosion resistance of the TCC-Zn55Al in chloride-containing solution could be significantly improved by appropriate pulse external electric field. Besides, Table 5 lists the values of each physical element obtained by EIS equivalent circuit fitting progress. When the pulse potential φ_p=−0.10 V, the value of $R_{pore,\ sol}$+R_{ct} was the largest, increases by 2.69 times compared with that without φ_p regulation. At the same time, when φ_p=−0.10 V, the C_{dl} value obtained by fitting appropriately increased, which indicated the smaller distance of the double layer capacitance between the sample surface and the electrolyte and this could also due to the increase of the surface micro-roughness leading to the larger contact area with the electrolyte. The EIS results indicated the changes in the internal structure of TCC. From the results of the above electrochemical measurements, the physical barrier effect of TCC on corrosive electrolyte became better under the effect of cathode φ_p. Of course, whether this corrosion resistance can be maintained with the increase of corrosion time is worthy of further study.

4 Discussion

As mentioned, it has been proven that the application of cathode φ_p has more positive effect on the corrosion resistance and surface property regulation of fresh formed TCC. And the effect of φ_p regulation can be maximized by adjusting its polarity and amplitude. More importantly, the application of φ_p further reduced the content of trace Cr(VI) on fresh formed TCC, which improved the environmental friendliness of freshly-formed TCC.

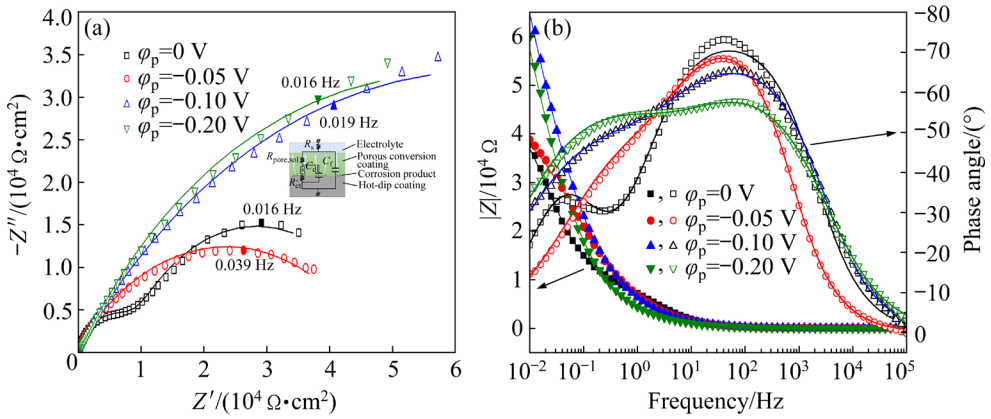

Fig. 11 EIS results of TCC in 0.5 mol/L NaCl solution regulated by cathode φ_p during TCP: (a) Nyquist diagram; (b) Bode diagram

Table 5 EIS fitting results of TCC regulated by anodic φ_p during TCP

φ_p/V	R_s/ (Ω·cm²)	$R_{pore,sol}$/ (Ω·cm²)	C_f/ (μF·cm⁻²)	R_{ct}/ (Ω·cm²)	C_{dl}/ (μF·cm⁻²)	W/ (μΩ⁻¹·s$^{0.5}$)
0	21.87	1.09×10⁴	11.97	3.78×10⁴	241.07	−
−0.05	44.22	5.51×10³	10.85	4.19×10⁴	65.15	−
−0.10	20.27	7.02×10³	14.68	1.24×10⁵	128.55	−
−0.20	20.71	4.31×10³	21.50	1.12×10⁵	68.29	−
+0.05	19.05	1.19×10⁴	6.67	3.01×10⁴	21.44	898
+0.10	18.22	7.39×10³	8.49	1.52×10⁴	111.33	−
+0.20	19.40	1.00×10⁴	10.07	9.46×10³	44.04	712

The Chi-Squared χ^2 of the fitting results is 0.014−0.017, and the estimated error is under 10%

4.1 Effective φ_p regulation on surface micro−nano structure

Due to the continuous increase of pH detected during the TCP, the generation of hydroxyl ion revealed in Reactions (1)−(3) was proven as the main driving force. As shown in Fig. 12, by applying the cathode φ_p, the construction speed of TCC was directly improved, and one important effect of pulse potential was reflected in the elimination of mass transfer barriers near the TCC-forming points. As a result, φ_p regulation reduced the size and number of micro cracks on the surface of TCC and improved the density of TCC by adjusting its micro−nano structure, which made TCC have better corrosion resistance in later aging and corrosion environment. The detailed average potential gradient distribution was revealed by the SVET measurement. The result in Fig. S5 in SI further indicated the cathode φ_p provided better uniformity of the potential distribution, which was consistent with the phenomenon that the surface of TCC became denser and the macro roughness decreased with the regulation of φ_p.

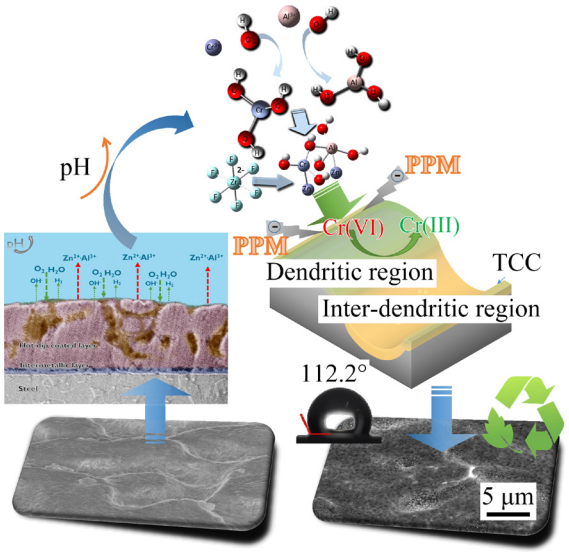

Fig. 12 Schematic diagram of regulation mechanism of TCC construction by φ_p on Zn55Al (PPM−Pulse potential method)

Figure 7 revealed the variation of micro-roughness of Zn55Al samples with and without the effect of φ_p. Based on the result of contact angle and coating adhesion strength measurement, the calculation of surface free energy was also carried out in this work. Figure 13 reveals the relationship among micro-roughness, adhesive strength, hydrophobicity and the surface free energy. It can be seen from Fig. 13 that the bonding strength between the Zn55Al surface and the epoxy primer was increased by 18.52% when φ_p was −0.05 V. In addition, when φ_p=−0.05 V and −0.10 V, the fracture presented a cohesive style, while that of degreased sample and samples with poor adhesion strength presented an adhesive style [47]. It was proven that the increase of micro-roughness and the decrease of macro-roughness worked together and improved the free energy on Zn55Al surface, which could be obtained by measuring the contact angle (θ) using pure water or glycerol and solving the equation [47,48]:

$$\gamma_{lv}\left(1+\cos\theta\right)=2\sqrt{\gamma_{sv}^{d}\gamma_{lv}^{d}}+2\sqrt{\gamma_{sv}^{p}\gamma_{lv}^{p}} \quad (7)$$

where γ_{lv} is the liquid surface energy, γ_{sv}^{p} and γ_{lv}^{p} are the polar components of the solid surface energy (term to be solved) and the liquid surface energy, respectively, while γ_{sv}^{d} and γ_{lv}^{d} (known items) are the dispersion components of the solid surface energy and the liquid surface energy, respectively.

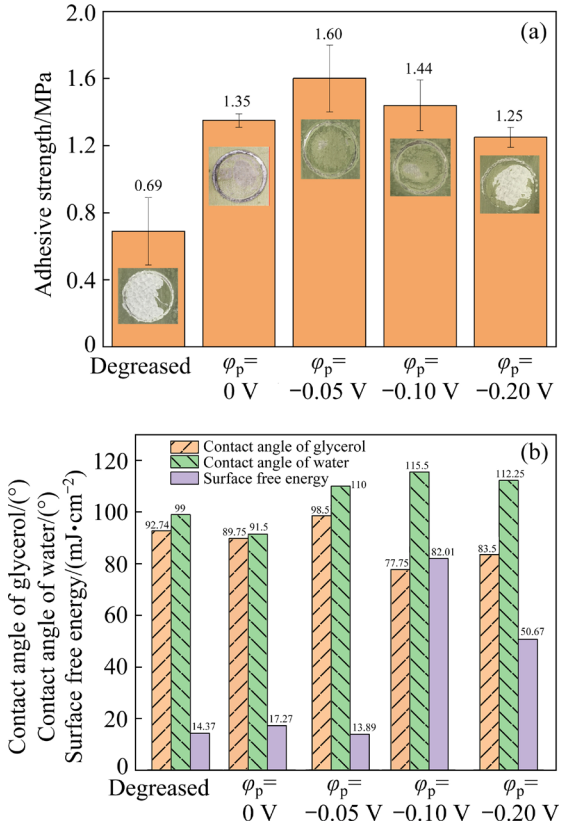

Fig. 13 Relationship among micro-roughness, adhesive strength, hydrophobicity and surface free energy on surface of TCC regulated by φ_p: (a) Variation of adhesive strength to epoxy primer; (b) Variations of adhesive strength, contact angle and surface free energy

4.2 Effective φ_p regulation on surface chemical composition

Previous studies about aluminum alloy have reported the double-layer structure of TCC [18,49]. The change of Cr/Zr molar ratio with the depth of TCC was calculated, as shown in Fig. S6 in SI. Compared with Zr, the content of Cr in the inner layer of TCC on Zn55Al surface was lager, while Zr was widely distributed at the middle depth of the TCC (mainly $ZrO_2{\cdot}2H_2O$).

Combined with the XPS analysis of fresh constructed TCC and previous studies on aluminum alloys, trace amount of hexavalent chromium is easy to appear at least on the surface of TCC, which may lead to the problem of usage limitation. The popular view is that in the process of TCP or corrosion, hydrogen peroxide generated by two electron reduction processes of oxygen on the surface of some cathode secondary phase oxidizes trivalent chromium to hexavalent chromium [49,50].

Two electron reduction reactions of oxygen:

$$O_2+2H_2O+2e\rightarrow H_2O_2+2OH^- \quad (8)$$

Formation of hexavalent chromium:

$$2Cr(OH)_3+3H_2O_2+4OH^-\rightarrow 2CrO_4^{2-}+8H_2O \quad (9)$$

Of course, this is possible because the micro cracks on TCC let the corrosion media especially the oxidation components reach the interface of the hot-dip coating through some narrow channels [51]. Whatever the reason, hexavalent chromium was detected on the surface of the fresh constructed TCC in this work, which was a more noteworthy conclusion. Although hexavalent chromium has a certain self-healing property in TCC, as shown in Reactions (10) and (11), the requirement of environmental protection regulations is more stringent [52]. However, during the process of TCP, the main cathode reaction on zinc rich region is 4-electron oxygen reduction. Due to the complex formation of hydrogen peroxide in acid medium, the appearance of hexavalent chromium needs to be further investigated [53].

Net redox reaction:

$$Al+CrO_4^{2-}+5H^+\rightarrow Cr(OH)_3+H_2O+Al^{3+} \quad (10)$$

Consumption of electrons at corroding site:

$$CrO_4^{2-}+5H^++3e\rightarrow Cr(OH)_3+H_2O \quad (11)$$

Despite the pressure of the environmental protection, the role of trivalent chromium in TCC is still irreplaceable. Based on equilibrium calculations, it was determined that Cr(VI) oxidizing substance reduction to trivalent chromium with higher reduction potential (Reactions (12) and (13) was thermodynamically feasible promoted, especially under the influence of cathode potential [54,55]:

$$Cr_2O_7^{2-}+14H^++6e\rightleftharpoons 2Cr^{3+}+7H_2O,\ \varphi^0=+1.39\ V \quad (12)$$

$$HCrO_4^{2-}+7H^++3e\rightleftharpoons Cr^{3+}+4H_2O,\ \varphi^0=+1.38\ V \quad (13)$$

The Raman shift positions given in Fig. 14 clearly reflected the key fingerprint information of Cr(III)—O and Cr(VI)—O even though this cannot be regarded as a quantitative indicator of the Cr(III)/Cr(VI) ratio. The spectra clearly reflected that the peak of Cr(VI)—O bands (i.e. CrO_4^{2-}, $HCrO_4^-$ and $Cr_2O_7^{2-}$, depending on the local pH) positioned at 840−904 cm^{-1} decreased, which easily distinguished them from the Cr(III)—O bands at 520 cm^{-1} (i.e. $Cr(OH)_3$) [49]. Of course, the local pH information during the TCP is also important. New local pH detection methods are studied, which can further guide the study of hexavalent chromium substance reduced during φ_p regulation.

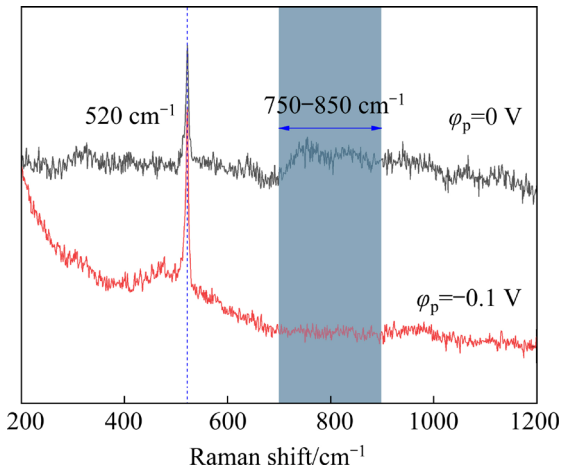

Fig. 14 Raman spectra of surface of freshly-formed TCC with φ_p=−0.1 V and φ_p=0 V

5 Conclusions

(1) The content of Cr(VI) on the surface of TCC-constructed Zn55Al was reduced after being regulated by square wave φ_p. When cathode φ_p= −0.20 V, the content of Cr(VI) in TCC was further

reduced by 30.20%. Cathode φ_p increased the content of OH^- on TCC by 52.46%, which was believed to effectively improve the adhesion of primer. The proportion of other main film-forming elements on TCC was also increased at the same time. The corrosion resistance in 0.5 mol/L NaCl solution was significantly improved and the regulation of cathode φ_p was better than that of anode.

(2) The crack sensitivity of TCC was high, especially at the transition region of dendrite region and interdendritic region. AES depth analysis showed that TCC had multilayer structure, the thickness of TCC at interdendritic region (~450 nm) was greater than that at dendritic region (~350 nm), and the depth of surface micro cracks could be equivalent to that of the TCC.

(3) When the cathode φ_p was applied, the micro-roughness of the TCC surface was further increased and the macro roughness decreased. The density and integrity of the TCC were improved while the micro cracks were reduced. The results provided guiding significance for developing the next generation conversion coating technology and breaking through the environmental protection barriers in the field of using TCP surface treatment.

Acknowledgments

The authors appreciate financial support from the National Natural Science Foundation of China (No. 51979282) and the Fundamental Research Funds for the Central Universities of China (No. 27RA2108004). The authors would like to acknowledge Research Director Dr. Vincent VIVIER at CNRS–Sorbonne University for his discussion and revision.

Supporting Information

Supporting Information in this paper can be found at: http://tnmsc.csu.edu.cn/download/14-p6067-2022-0290-Supporting_Information.pdf.

References

[1] MOREIRA A R, PANOSSIAN Z, CAMARGO P L, MOREIRA M F, da SILVA I C, de CARVALHO J R. Zn/55Al coating microstructure and corrosion mechanism [J]. Corrosion Science, 2006, 48: 564−576.

[2] BLICKWEDE D J. 55%Al−Zn-alloy-coated sheet steel [J]. Tetsu-to-Hagané, 1980, 66(7): 821−834.

[3] LU Jin-tang, WANG Xin-hua, CHE Chun-shan, KONG Gang, CHEN Jin-hong, XU Qiao-yu. Crystallographic research of spangle on hot dip galvanized steel sheets [J]. Transactions of Nonferrous Metals Society of China, 2007, 17(2): 351−356.

[4] ZHANG X, VU T N, VOLOVITCH P, LEYGRAF C, OGLE K, WALLINDER I O. The initial release of zinc and aluminum from non-treated galvalume and the formation of corrosion products in chloride containing media [J]. Applied Surface Science, 2012, 258(10): 4351−4359.

[5] VU T N, VOLOVITCH P, OGLE K. The effect of pH on the selective dissolution of Zn and Al from Zn−Al coatings on steel [J]. Corrosion Science, 2013, 67: 42−49.

[6] HAN J, THIERRY D, OGLE K. Zr-based conversion coating on Zn and Zn−Al−Mg alloy coating: Understanding the accelerating effect of Cu(II) and NO_3^- [J]. Surface and Coatings Technology, 2020, 402: 126236.

[7] PHUONG N V, GUPTA M, MOON S. Enhanced corrosion performance of magnesium phosphate conversion coating on AZ31 magnesium alloy [J]. Transactions of Nonferrous Metals Society of China, 2017, 27(5): 1087−1095.

[8] PALMA E, PUENTE J M, MORCILLO M. The atmospheric corrosion mechanism of 55%Al−Zn coating on steel [J]. Corrosion Science, 1998, 40: 61−68.

[9] VU A Q, VUILLEMIN B, OLTRA R, ALLÉLY, C. Cut−edge corrosion of a Zn−55Al−coated steel: A comparison between sulphate and chloride solutions [J]. Corrosion Science, 2011, 53: 3016−3025.

[10] LOWE T A, WALLACE G G, NEUFELD A K. Insights into the cut edge corrosion of 55%Al−Zn metal coating on steel from simultaneous electrochemical polarization and localised pH sensing experiments [J]. Corrosion Science, 2012, 55: 180−186.

[11] QIU P, LEYGRAF C, ODNEVALL WALLINDER I. Evolution of corrosion products and metal release from Galvalume coatings on steel during short and long-term atmospheric exposures [J]. Materials Chemistry and Physics, 2012, 133(1): 419−428.

[12] LIU Y, OOI A, TADA E, NISHIKATA, A. Electrochemical monitoring of the degradation of galvanized steel in simulated marine atmosphere [J]. Corrosion Science, 2019, 147: 273−282.

[13] YADAV A P, KATAYAMA H, NODA K, MASUDA H, NISHIKATA A, TSURU T. Effect of Al on the galvanic ability of Zn−Al coating under thin layer of electrolyte [J]. Electrochimica Acta, 2007, 52 (7): 2411−2422.

[14] MILOŠEV I, FRANKEL G S. Review−Conversion coatings based on zirconium and/or titanium [J]. Journal of the Electrochemical Society, 2018, 165(3): C127−C144.

[15] KENDIG M W, BUCHHEIT R G. Corrosion inhibition of aluminum and aluminum alloys by soluble chromates, chromate coatings, and chromate-free coatings [J]. Corrosion, 2003, 59(5): 379−400.

[16] KOZADEROV O, ŚWIATOWSKA J, DRAGOE D, BURLIAEV D, VOLOVITCH P. Effect of Cr(III) passivation layer on surface modifications of zinc–nickel coatings in chloride solutions [J]. Journal of Solid State Electrochemistry, 2021, 25(4): 1161−1173.

[17] ŠEKULARAC G, KOVAČ J, MILOŠEV I. Comparison of

the electrochemical behaviour and self-sealing of zirconium conversion coatings applied on aluminium alloys of series 1xxx to 7xxx [J]. Journal of the Electrochemical Society, 2020, 167(11): 111506.

[18] SAILLARD R, ZANNA S, SEYEUX A, FORI B, ŚWIATOWSKA J, BLANC C, MARCUS P. Influence of ageing on the corrosion behaviour of 2024 aluminium alloy coated with a trivalent chromium conversion layer [J]. Corrosion Science, 2021, 182: 109192.

[19] RAMEZANZADEH B, ATTAR M M. An evaluation of the corrosion resistance and adhesion properties of an epoxy-nanocomposite on a hot-dip galvanized steel (HDG) treated by different kinds of conversion coatings [J]. Surface and Coatings Technology, 2011, 205: 4649−4657.

[20] PAN J, TANG X, LI Y. Influence of treatment time on performance of Cr(III)-based conversion coatings on hot dip Zn−55Al−1.6Si coated steel sheet [J]. Coatings, 2019, 9(5): 297.

[21] LOSTAK T, TIMMA C, KREBS S, FLOCK J, SCHULZE S. Organosilane modified Zr-based conversion layer on Zn−Al alloy coated steel sheets [J]. Surface and Coatings Technology, 2016, 305: 223−230.

[22] LIU Q, ZHANG X R, SANG Y L, DU A, MA R N, ZHAO X, FAN Y Z, CAO X M. Corrosion resistance and adhesion behavior of an octa-(aminopropyl) polyhedral oligomeric silsesquioxane-modified graphene oxide-incorporated conversion coating for hot-dip galvanized steel [J]. Surface and Coatings Technology, 2021, 409: 126900.

[23] ZENG Rong-chang, HU Yan, ZHANG Fen, HUANG Yuan-ding, WANG Zhen-lin, LI Shuo-qi, HAN En-hou. Corrosion resistance of cerium-doped zinc calcium phosphate chemical conversion coatings on AZ31 magnesium alloy [J]. Transactions of Nonferrous Metals Society of China, 2016, 26(2): 472−483.

[24] ZHANG S H, KONG G, LU J T, CHE C S, LIU L Y. Growth behavior of lanthanum conversion coating on hot-dip galvanized steel [J]. Surface and Coatings Technology, 2014, 259: 654−659.

[25] LI L, SWAIN G P, HOWELL A, WOODBURY D, SWAIN G M. The formation, structure, electrochemical properties and stability of trivalent chrome process (TCP) coatings on AA2024 [J]. Journal of the Electrochemical Society, 2011, 158(9): C274−C283.

[26] STOICA A I, ŚWIATOWSKA J, ROMAINE A, DI FRANCO F, QI J, MERCIER D, SEYEUX A, ZANNA S, MARCUS P. Influence of post-treatment time of trivalent chromium protection coating on aluminium alloy 2024−T3 on improved corrosion resistance [J]. Surface and Coatings Technology, 2019, 369: 186−197.

[27] VERDALET-GUARDIOLA X, BONINO J P, DULUARD S, FORI B, BLANC C. Influence of the alloy microstructure and surface state on the protective properties of trivalent chromium coatings grown on a 2024 aluminium alloy [J]. Surface and Coatings Technology, 2018, 344: 276−287.

[28] WALTON J, SHRUTHI T K, YANCEY D, VLASAK P, WESTRE S, SWAIN G M. Evaluation of a trivalent chromium process (TCP) conversion coating on AA2024-T3 that requires no surface pretreatment [J]. Journal of the Electrochemical Society, 2019, 166(15): C589−C599.

[29] GUO Y, FRANKEL G S. Characterization of trivalent chromium process coating on AA2024-T3 [J]. Surface and Coatings Technology, 2012, 206: 3895−3902.

[30] CHANG Y T, WEN N T, CHEN W K, GER M D, PAN G T, YANG T C K. The effects of immersion time on morphology and electrochemical properties of the Cr(III)-based conversion coatings on zinc coated steel surface [J]. Corrosion Science, 2008, 50: 3494−3499.

[31] VERDALET-GUARDIOLA X, FORI B, BONINO J P, DULUARD S, BLANC C. Nucleation and growth mechanisms of trivalent chromium conversion coatings on 2024-T3 aluminium alloy [J]. Corrosion Science, 2019, 155: 109−120.

[32] CACHET C, GANNE F, MAURIN G, PETITJEAN J, VIVIER V, WIART R. EIS investigation of zinc dissolution in aerated sulfate medium. Part I: Bulk zinc [J]. Electrochimica Acta, 2001, 47: 509−518.

[33] ASEMANI H R, AHMADI P, SARABI A A, MOHAMMADLOO H E. Effect of zirconium conversion coating: adhesion and anti-corrosion properties of epoxy organic coating containing zinc aluminum polyphosphate (ZAPP) pigment on carbon mild steel [J]. Progress in Organic Coatings, 2016, 94: 18−27.

[34] LI L, DESOUZA A L, SWAIN G M. In situ pH measurement during the formation of conversion coatings on an aluminum alloy (AA2024) [J]. Analyst, 2013, 138: 4398−4402.

[35] SARFRAZ A, POSNER R, LANGE M M, LILL K, ERBE A. Role of intermetallics and copper in the deposition of ZrO_2 conversion coatings on AA6014 [J]. Journal of the Electrochemical Society, 2014, 161(12): C509−C516.

[36] GEORGE F O, SKELDON P, THOMPSON G E. Formation of zirconium-based conversion coatings on aluminium and Al−Cu alloys [J]. Corrosion Science, 2012, 65: 231−237.

[37] MUNSON C A, SWAIN G M. Structure and chemical composition of different variants of a commercial trivalent chromium process (TCP) coating on aluminum alloy 7075-T6 [J]. Surface and Coatings Technology, 2017, 315: 150−162.

[38] National Institute of Standards and Technology. NIST X-ray photoelectron spectroscopy database [DB/OL]. Gaithersburg MD, 2000, 20899. doi:10.18434/T4T88K.

[39] ALLEN G C, CURTIS M T, HOOPER A J, TUCKER P M. X-ray photoelectron spectroscopy of chromium-oxygen systems [J]. Journal of the Chemical Society, Dalton Transactions, 1973(16): 1675−1683.

[40] MOFFAT T P, LATANISION R M. An electrochemical and X-ray photoelectron spectroscopy study of the passive state of chromium [J]. Journal of the Electrochemical Society, 1992, 139(7): 1869−1879.

[41] PAN J, TANG X, LI Y. Pulse potential method-assisted construction and regulation of a trivalent chromium conversion coating on hot-dip coated steel sheet [J]. Corrosion Science, 2020, 176: 109026.

[42] SLEIGH C, PIJPERS A P, JASPERS A, COUSSENS B, MEIER R J. On the determination of atomic charge via ESCA including application to organometallics [J]. Journal of Electron Spectroscopy and Related Phenomena, 1996, 77(1): 41−57.

[43] SABABI M, TERRYN H, MOL J M C. The influence of a

Zr-based conversion treatment on interfacial bonding strength and stability of epoxy coated carbon steel [J]. Progress in Organic Coatings, 2017, 105: 29−36.
[44] FOCKAERT L I, TAHERI P, ABRAHAMI S T, BOELEN B, TERRYN H, MOL J M C. Zirconium-based conversion film formation on zinc, aluminium and magnesium oxides and their interactions with functionalized molecules [J]. Applied Surface Science, 2017, 423: 817−828.
[45] STERN M, GEARY A L. Electrochemical polarization I. a theoretical analysis of the shape of polarization curves [J]. Journal of the Electrochemical Society, 1957, 104(1): 56−63.
[46] ALMEIDA E, FEDRIZZI L, DIAMANTINIO T C. Oxidising alternative species to chromium VI in zinc-galvanised steel surface treatment. Part 2−An electro-chemical study [J]. Surface and Coatings Technology, 1998, 105: 97−101.
[47] ZHU W, LI W, MU S, YANG Y, ZUO X. The adhesion performance of epoxy coating on AA6063 treated in Ti/Zr/V based solution [J]. Applied Surface Science, 2016, 384: 333−340.
[48] VAKILI H, RAMEZANZADEH B, AMINI R. The corrosion performance and adhesion properties of the epoxy coating applied on the steel substrates treated by cerium-based conversion coatings [J]. Corrosion Science, 2015, 94: 466−475.
[49] LI L, KIM D Y, SWAIN G M. Transient formation of chromate in trivalent chromium process (TCP) coatings on AA2024 as probed by raman spectroscopy [J]. Journal of the Electrochemical Society, 2012, 159(8): C326−C333.
[50] SHRUTHI T K, SWAIN G M. Detection of H_2O_2 from the reduction of dissolved oxygen on TCP-coated AA2024-T3: Impact on the transient formation of Cr(VI) [J]. Journal of the Electrochemical Society, 2019, 166(11): C3284−C3289.
[51] EARY L E, RAI D. Kinetics of chromium(III) oxidation to chromium(VI) by reaction with manganese dioxide [J]. Environmental Science & Technology, 1987, 21(12): 1187−1193.
[52] LUNDER O, WALMSLEY J C, MACK P, NISANCIOGLU K. Formation and characterisation of a chromate conversion coating on AA6060 aluminium [J]. Corrosion Science, 2005, 47: 1604−1624.
[53] JIANG Y Y, NI P J, CHEN C X, LU Y Z, YANG P, KONG B, FISHER A, WANG X. Selective electrochemical H_2O_2 production through two-electron oxygen electrochemistry [J]. Advanced Energy Materials, 2018, 8(31): 1801909.
[54] APTE A D, VERMA S, TARE V, BOSE P. Oxidation of Cr(III) in tannery sludge to Cr(VI): Field observations and theoretical assessment [J]. Journal of Hazardous Materials, 2005, 121(1/2/3): 215−222.
[55] HESAMEDINI S, BUND A. Formation of Cr(VI) in cobalt containing Cr(III)-based treatment solution [J]. Surface and Coatings Technology, 2018, 334: 444−449.

方波电位幅值和极性对锌铝合金热浸镀层表面三价铬化学转化膜性能的影响

潘 杰，程 洋，丁雅静，赵瑞程，蒋 涛，冯振亮，李 焰

中国石油大学(华东) 材料科学与工程学院，青岛 266580

摘 要：揭示热浸镀锌铝合金镀层表面 Cr(III)化学转化膜(TCC)的构建过程，对比研究阴极和阳极方波电位(φ_p)改善转化膜性能的作用效果。通过 EIS 和极化曲线测试获得 TCC 在含氯离子介质中的耐蚀性。结合表面宏/微观 3D 形貌观察和 XPS、AES、FTIR 以及拉曼光谱等化学组分分布分析，系统讨论耐蚀性提升与表面组织结构之间的联系。结果表明，阴极方波电位 φ_p 相较阳极电位在提高 TCC 耐蚀性和降低 TCC 表面 Cr(VI)含量方面的作用更为显著。另外，由于微纳结构的重构，TCC 的疏水性以及与环氧底漆之间的结合力得到提升。

关键词：热浸镀层；Cr(III)化学转化膜；方波电位；表面粗糙度

(Edited by Bing YANG)